Materials Today Bio 28 (2024) 101209

Contents lists available at ScienceDirect

Materials Today Bio

journal homepage: www.journals.elsevier.com/materials-today-bio

NIR laser-activated phthalocyanine loaded lipid nanoparticles targeting M2 macrophage for improved photoacoustic imaging-guided photothermal therapy

Xingzhou Peng [a,1], Junjie Wang [b,c,1], Zihan Deng [d,1], Jianshuang Wei [b], Changqiang Xie [a], Yan Wang [a], Jianlei Han [e], Zhengyu Chen [a], Jianghai Du [a], Zhihong Zhang [a,b,*]

[a] State Key Laboratory of Digital Medical Engineering, Key Laboratory of Biomedical Engineering of Hainan Province, School of Biomedical Engineering, Hainan University, Sanya, Hainan, 572025, China
[b] Britton Chance Center and MoE Key Laboratory for Biomedical Photonics, Wuhan National Laboratory for Optoelectronics, Huazhong University of Science and Technology, Wuhan, Hubei, 430074, China
[c] Key Laboratory of Emergency and Trauma, Ministry of Education, Key Laboratory of Hainan Trauma and Disaster Rescue, The First Affiliated Hospital of Hainan Medical University, Engineering Research Center for Hainan Bio-Smart Materials and Bio-Medical Devices, Hainan Medical University, Haikou, 571199, China
[d] Department of Thoracic Surgery, ZhongNan Hospital of Wuhan University, Wuhan, Hubei, 430074, China
[e] CAS Center for Excellence in Nanoscience, CAS Key Laboratory of Nanosystem and Hierarchical Fabrication, Beijing, 100190, China

ARTICLE INFO

Keywords:
Breast cancer
M2 macrophage
Ruthenium phthalocyanine
Photothermal therapy
Deep penetration

ABSTRACT

The development of novel phototheranostic agents with significant potential in bioimaging-guided therapy is highly desirable for precise tumor therapy. Herein, NIR laser-activated ruthenium phthalocyanine (PcRu) loaded sub-30 nm targeting lipid nanoparticles (α-PcRu-NPs) were fabricated for photoacoustic imaging (PAI)-guided photothermal therapy (PTT). Due to the formation of *J*-type aggregation of PcRu in the core of the nanostructure, the α-PcRu-NPs exhibited high stability, efficient NIR absorption, reduced singlet oxygen generation, high photothermal activity, and intense photoacoustic signal. With the M2 macrophage target peptide (M2pep) modification and small size of α-PcRu-NPs, *in vivo* evaluations reveal that α-PcRu-NPs can specifically target and deeply penetrate the tumor foci. Under a high contrast PAI guidance with α-PcRu-NPs (744 nm, 0.35 μW), it also realizes superior photothermal therapy (PTT) for breast cancer under 670 nm laser irradiation (0.5 W/cm^2). The prominent therapeutic efficacy of α-PcRu-NP-based PTT not only directly kills tumor cells, but also enhances the immune response by promoting dendritic cell maturation and increasing cytotoxic T cell infiltration. Thus, this work broadens the applications of phthalocyanine derivatives as phototheranostics in the PAI-guided PTT field.

1. Introduction

Malignant tumors have surpassed cardiovascular diseases in terms of mortality, posing a major hazard to human health and life [1,2]. Surgery, chemotherapy and radiation therapy are the current first-line cancer therapies in the clinic [3,4]. However, the challenge of the low cure rate and high risk of tumor recurrence and metastasis still exists [5,6]. The introduction of novel technologies in clinical settings, such as immune checkpoint therapy and CAR-T cell therapy, demonstrates the capability to avoid the issues encountered by conventional treatments and successfully improve the efficacy of disease treatment [7,8]. Additionally, phototherapy, encompassing photothermal therapy (PTT) and photodynamic therapy (PDT), has garnered significant interest for its capacity to elicit direct tumor destruction and trigger anti-tumor immune reactions, rendering it a highly promising modality for tumor treatment with substantial clinical utility [4]. However, phototherapy often encounters side effects like tissue damage due to exposure to laser irradiation. To minimize such potential side effects, imaging-guided PTT or PDT for tumor treatment becomes especially crucial [9].

The combination of photoacoustic imaging and photothermal therapy (PAI/PTT) has been considered as a promising phototheranostic system because of the accurate diagnosis and efficient inhibition of

* Corresponding author. Key Laboratory of Biomedical Engineering of Hainan Province, School of Biomedical Engineering, Hainan University, Sanya, Hainan, 572025, China.
E-mail address: zhzhang@hainanu.edu.cn (Z. Zhang).
[1] These authors contributed equally to this work.

https://doi.org/10.1016/j.mtbio.2024.101209
Received 16 May 2024; Received in revised form 14 August 2024; Accepted 23 August 2024
Available online 24 August 2024

cancer development [10,11]. The PAI is a hybrid imaging modality that provides high-resolution, deep-tissue imaging with excellent contrast and sensitivity, making it valuable for various medical applications such as cancer detection, vascular imaging, and functional brain imaging [12,13]. Additionally, it is non-invasive and uses non-ionizing radiation, endowing it with superior safety [14,15]. Similarly, PTT also depends on the conversion of pulsed-light energy to thermal expansion, which can non-invasively abolish the tumor, then release whole tumor-antigen to trigger a strong anti-tumor response [16–18]. As both PAI and PTT are based on the photothermal-activatable principle, phototheranostic agents (PTAs) with good biocompatibility, good photostability, red-shifted absorption in the NIR window, and high photothermal conversion efficiency (PCE) are prerequisites for strong PA signal and enhanced PTT efficiency for solid tumors [19,20].

Phthalocyanine (Pc) is a type of aromatic heterocycle compound with four nitrogen-bridged isoindoles constructed, which harness strong absorption ability in the NIR region ($\lambda_{max} > 660$ nm, $\varepsilon_{max} > 10^5$ $M^{-1}cm^{-1}$) and adjustable photochemical properties through facile chemical modifications [21,22]. Compared with clinically used porphyrins, Pcs show low absorption in visible wavelength (400–600 nm), which can reduce the skin photosensitivity activated by sunlight [23,24]. Most of Pcs have been extensively explored as photosensitizers for photodynamic therapy (PDT) due to low fluorescence emission [22,25–28]. Recently, more attention has been paid on the exquisite design and improvement of Pcs as PAI/PTT contrast agents [29]. To enhance the photothermal activity, the metal atom is typically integrated into the core of the phthalocyanine molecule. The inclusion of ruthenium has been confirmed to significantly improve both the absorption in the near-infrared spectrum and the molecular photostability [30]. Meanwhile, the ruthenium, known as major moiety of the second-generation metal-based chemotherapeutics, has been clinically considered safer than platinum making it promising in biomedical applications [30]. To solve the solubility of Pcs under physiological conditions, chemical modification and nanostructure construction are recognized as effective strategies. Li et al. designed a supramolecular phthalocyanine (PcS4-PcN4) *via* the self-assembly of two water-soluble compounds (PcS4 and PcN4) with high photoacoustic and photothermal activity [31]. In addition, encapsulation of phosphorus Pcs (P-Pcs) in the liquid surfactants [32] or binding of cationic amphiphilic phthalocyanine into liposome layers [33] have been used for deep PA imaging and cancer phototherapy, respectively. However, delivery of Pcs/drugs to tissue and cells with poor selectivity is still a challenge, which hinders clinical translation. In our previous report, a biomimetic nano-system modified with a fused peptide (FAEKFKEAVKDYFAKFWS-GSG-WEDYQWPVYKGW) was successfully formulated to deliver the siRNA. Two target peptide moieties were designed for this fused peptide, one is an R4F peptide (FAEKFKEAVKDYFAKFWS) bounded with SR-B1$^+$ cells, the other is a specific M2-like macrophage binding peptide (WEDYQWPVYKGW). With this dual-targeted peptide modification, the nanoparticle exhibited effective target ability to M2-like tumor-associated macrophages (TAM). After loading anti-colony stimulating factor-1 receptor (anti-CSF-1R) siRNA, this nanomedicine can deplete M2-like TAM and

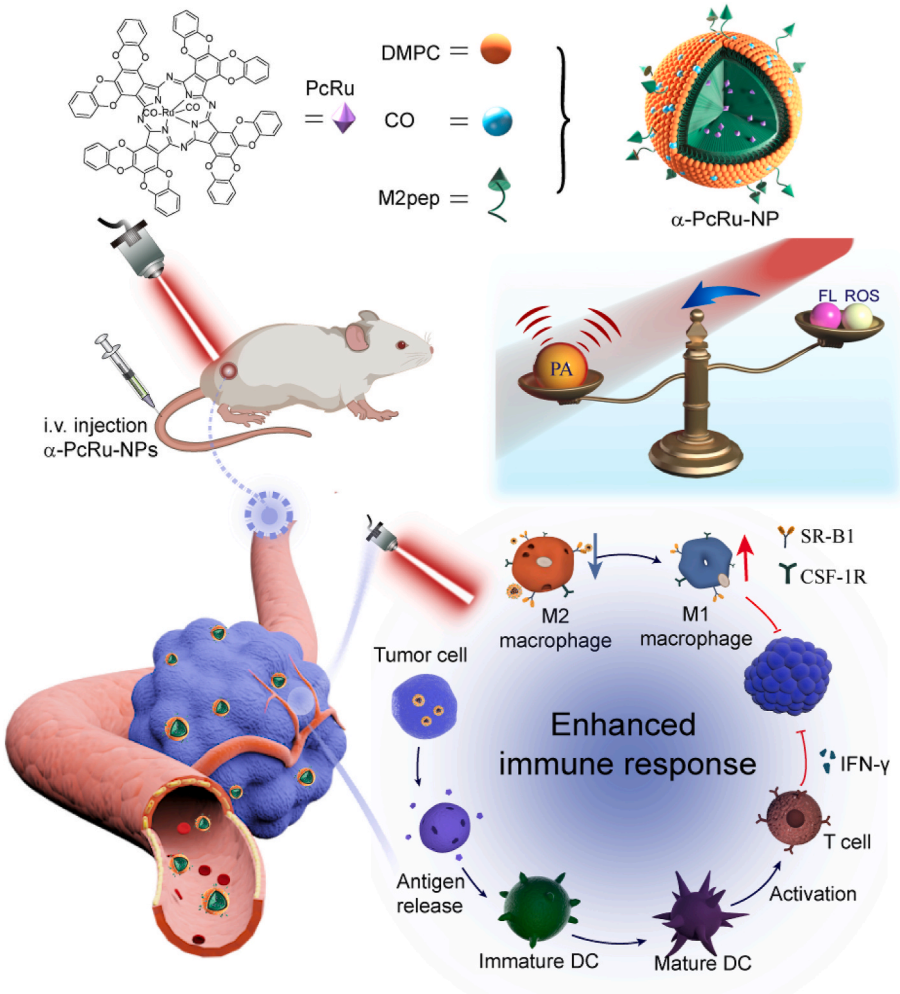

Scheme 1. Schematic illustration for the preparation of α-PcRu-NPs and their applications in photoacoustic imaging-guided photothermal therapy, accompanied by enhancement of immune responses.

then inhibit tumor growth, resulting in enhanced anti-tumor effect [34]. Besides, the small size of this nano platform also helped siRNA deep penetration into solid tumors to achieve satisfactory treatment effects. Therefore, the development of novel phototheranostic agents with multifunctional nano-systems is highly desirable for efficient anti-tumor therapy.

Herein, a novel ruthenium phthalocyanine (PcRu) with extended π-electron through two benzodioxin linkages endows better solubility and red-shifted absorption spectra to the NIR region was designed, which can be expected as an excellent candidate as PAI/PTT agent. Then PcRu was further loaded into biomimetic nanoparticle, namely α-PcRu-NPs, endowing it with tumor and M2 macrophage dual-targeting and deep tumor penetration features (Scheme 1). *In vitro* and *in vivo* evaluation of the fluorescence, photoacoustic and photothermal properties revealed that α-PcRu-NPs combined with fluorescence emission suppression and reduced singlet oxygen formation resulted in a high level of photoacoustic and photothermal activity. Notably, α-PcRu-NPs may effectively concentrate in intratumor blood vessels and tumor foci, which benefits the amplification of phototheronostics. As results, our developed PcRu and α-PcRu-NPs nanocomposites will be a powerful therapeutic agent for the PAI-guided PTT against solid tumors.

2. Materials and methods

2.1. Materials

1,2-dimyristoyl-sn-glycero-3-phosphocholine (DMPC), 1,2-distearoyl-sn-glycero-3-phosphoethanolamine-N-propyl ethylene glycol-2000 (DSPE-PEG_{2000}) were purchased from Avanti Polar Lipids Inc. (Alabaster, Alabama, USA). Cholesterol oleate (CO, 98 %) was obtained from Sigma-Aldrich Co. (St. Louis, MO, USA). Free M2pep with the sequence FAEKFKEAVKDYFAKFWS-GSG-WEDYQWPVYKGW was synthesized by Shanghai Apeptide Co. Ltd (Shanghai, China). All commercial reagents were used as received unless otherwise stated.

2.2. Synthesis of phthalonitrile compound 3 [35]

Catechol **1** (1.10 g, 10 mmol), tetrachlorophthalonitrile **2** (1.05 g, 4 mmol), potassium carbonate (1.38 g, 10 mmol), and DMF (25 mL) were heated to 100 °C under Ar for 1 h. After cooling to room temperature, the solids were filtered and washed with water (100 mL) then methanol (50 mL). The collected solids were dried under vacuum to yield a white powder **3** (1.26 g, 93 % yield).

2.3. Synthesis of PcRu

A mixture of phthalonitrile compound **3** (1.36 g, 4 mmol) and triruthenium dodecacarbonyl $Ru_3(CO)_{12}$ (256 mg) and 1,8-Diazabicyclo [5.4.0]undec-7-ene (DBU) (0.5 mL) in 1-octanol (60 mL) and DMF (12 mL), was refluxed for 36 h in Ar atmosphere. When cooled down to room temperature, the solution was dropped into methanol. The solid was washed with water, and then it was extracted by Soxhlet extractor with methanol till colorless. At last, the dark green product was purified by silica gel column chromatography using dichloromethane and ethanol as eluent. IR ν_{max}/cm^{-1}(KBr): 746, 975, 1147, 1251, 1309, 1434, 1590, 1964, 2014, 2052, 2850, 2919, 3064. MS (Maldi-TOF) *m/z*: calcd: 1518.27, found: 1518.45 $[M]^+$.

2.4. Prepare of α-PcRu-NP

A mixture of DMPC (3 μM), CO (0.1 μM), DSPE-PEG_{2000} (0.0114 μM), and PcRu (0.1 μM) was dissolved in chloroform and then dried under nitrogen for a uniform. The mixture was then hydrated with 1 mL water and sonicated for 1 h at 46 °C. The dissolved M2 peptide was added into the lipid emulsion to make α-PcRu-NP by overnight incubation at 4 °C. The nanoparticles were concentrated using a concentrator tube with a 30 kDa molecular weight cutoff.

2.5. Characterization

Mass spectral data were obtained by using a Solari X maldi-FTMS instrument. UV–vis absorption spectra were obtained using Hitachi U-3900 spectrophotometer. Fluorescence spectra were measured using F-4600 fluorescence spectrophotometer. The hydrodynamic size (DLS) and zeta potential data were obtained on a Zetasizer Nano-ZS90 (Malvern Instruments, Worcestershire, UK). The lipid-coated particles were prepared on the TEM grids with 2 wt% citric acid for negative staining and the images were obtained by using CrossBeam 350 TEM. The acoustic resolution photoacoustic microscopy (AR-PAM) system was used for all photoacoustic measurements. The AR-PAM system consists of a pump laser (532 nm), a dye laser (744 nm), a focused ultrasound transducer (central frequency: 50 MHz; fractional bandwidth: 49 MHz; N.A.:0.47), and a precision motorized 3D scanning stage. The lateral resolution of AR-PAM was measured to be 50 μm (theoretically calculated to be 45 μm) and the imaging depth reached 3 mm.

2.6. Loading efficiency and release of α-PcRu-NP

The α-PcRu-NP was ruptured by adding 1 % Triton X-100 and releasing free PcRu into water under sonication. The amount of PcRu in the supernatant was obtained by recording the UV–vis absorbance at 730 nm.

Encapsulation efficiency (%) $= \frac{m_{PcRu\ in\ nanoparitlces}}{m_{initial\ PcRu}} \times 100\ \%$

The release of PcRu from α-PcRu-NP was conducted by incubating α-PcRu-NP (PcRu concentration: 20 μM) in PBS at 37 °C and aliquoted into 18 tubes. At predetermined time intervals (0 h, 1 h, 3 h, 6 h, 24 h, 48 h), three parallel tubes were removed and centrifuged at 200000× g for 10 min. The supernatants were then collected for UV–vis absorbance detection by a microplate reader. The release percentage was calculated based on the relative absorption at 730 nm.

2.7. Reactive oxygen species (ROS) generation

The singlet oxygen ($^1O_2$) generation efficiency was tested in aqueous solution. 1,3-diphenylisobenzofuran (DPBF) was first dissolved in DMSO to give a 20 mM of solution, and then diluted with H_2O to 100 μM (containing 0.5 % DMSO). The DPBF solution (200 μL) was then mixed with PcRu or α-PcRu-NP ([DPBF] = 100 μM, [PcRu] = 10 μM). The mixture was irradiated with 670 nm laser immediately, and then DPBF degradation at 415 nm was monitored along with irradiated time.

To determine the hydroxyl radical (·OH) and superoxide anion ($\cdot O_2^-$) generation, aminophenyl fluorescein (APF) and dihydrorhodamine 123 (DHR 123) were used as indicator, respectively. The α-PcRu-NP ([PcRu] = 10 μM) was added to APF solution (10 μM) or DHR 123 solution (10 μM). The mixture was irradiated with 670 nm laser at different times. The fluorescence intensity of APF or DHR 123 were measured by the spectrofluorometer to analyze the content of ·OH (Ex: 460 nm, Em:515 nm) or $\cdot O_2^-$ (Ex: 500 nm, Em: 536 nm).

2.8. PA characterization of α-PcRu-NP

The photoacoustic characterization was conducted with a home-made acoustic-resolution photoacoustic microscopy system (AR-PAM) with a 744 nm laser. The laser energy was calibrated and optimized using an in-built energy meter before measurements. The tubing was then fixed onto a custom-made acrylic holder, suspended across the center of the bowl array, and immersed in water. The FL/PA spectral signature of each sample was determined by region of interest (ROI) analysis using Fiji software.

2.9. Photothermal measurements of α-PcRu-NP

The photothermal performance of α-PcRu-NP was systematically evaluated. α-PcRu-NP at different PcRu concentrations (0–20 μM, 200 μL) were irradiated with a 670 nm laser (0.5 W/cm^2) irradiation for 5 min, and a fixed concentration (5 μM) of α-PcRu-NP was irradiated at different laser intensities (0.5–1.5 W/cm^2). The temperature changes were recorded by a thermal imager. Each experiment was repeated three times. To obtain the photothermal conversion efficiency (η) for α-PcRu-NP solution, the heating curve of the samples was monitored. α-PcRu-NP solution was recorded upon 670 nm laser irradiation (0.5 W/cm^2) for 6 min to achieve the maximum plateau of temperature, and the laser was turned off for natural cooling to room temperature. Thus, η can be calculated by referring to Equation (1):

$$\eta = \frac{hS(T_{max} - T_{surr}) - Q_{diss}}{I\left(1 - 10^{A}\lambda\right)}$$

I is the laser power, A is the absorbance of the samples at 670 nm, $T_{\max}$ and T_{surr} denote the maximum steady-state temperature and room temperature, respectively; Q_{diss} is the heat wastage from the light loss of the solvent and holder; hS can be calculated according to Equation (2):

$$\tau_s = \frac{mC_p}{hS}$$

where τ_s is the time constant, m is the mass of the solution, C_p is the heat capacity of the corresponding solvent. Finally, the PCE can be calculated.

2.10. Cell culture and MTS assay

The 4T1 cells and RAW264.7 cells were incubated at 37 °C (5 % CO_2) in Dulbecco's Modified Eagle's Medium (DMEM, Hyclone) supplemented with 10 % (vol/vol) fetal bovine serum (Gibco) and 100 U mL^{-1} penicillin-streptomycin. Then RAW264.7 cells were treated with 20 ng/mL IL-4 for 24 h to acquire M2-like macrophages. The acquired cells were stained with anti-F4/80-AF488 (Biolegend, Clone BM8) and anti-CD206-PE (Biolegend, Clone C068C2) for 0.5 h and the phenotype of macrophages were detected by flow cytometer analysis.

The MTS assay was carried out to investigate the toxicity of the as-prepared NPs. In brief, 4T1 cells were seeded in a 96-well plate at a density of 1 × 10^4 cells/well and cultured overnight. The cells were incubated with serial PcRu concentrations (5, 10, 20 μM) of PcRu, PcRu-NP, α-PcRu-NP for 24 h then, the cells were washed with PBS and the medium was removed. Cytotoxicity was evaluated by a standard MTS assay.

Cell viability = ($OD_{490\ nm}$ of the experimental group/$OD_{490\ nm}$ of the control group) × 100 %, and the cell viability of the control group was denoted as 100 %.

2.11. Cells targeting ability and uptake efficiency

For confocal imaging, M2-like macrophages were seeded (2 × 10^5 cells/well) into 8-well chambers covering the glass bottoms (Nunc Lab-Tek, Thermo Scientific). The cells were then incubated with α-PcRu-NPs (DiR-BOA) and PcRu-NPs(DiR-BOA) (DiR-BOA: 1 μM) for 3 h, and Hoechst 33342 was added for nucleus staining. Fluorescence images were captured using a laser confocal scanning microscope Olympus FV3000 (Olympus, Japan) with an excitation wavelength of 405 nm for Hoechst 33342 and 640 nm for DiR-BOA.

For flow cytometry analysis of M2-like macrophages and 4T1 cell-targeting ability, M2-like macrophages or 4T1 cells were seeded into 48-well plates (5 × 10^4 cells/well), and α-PcRu-NPs(DiR-BOA) and PcRu-NPs(DiR-BOA) were incubated with the cells at different DiR-BOA concentrations (0.1, 1 and 10 μM) for 3 h or incubated for different time (1, 3 and 6 h) with the same DiR-BOA concentration (1 μM). The collected cells were analyzed using CytoFLEX flow cytometry (Beckman Coulter, USA).

2.12. In vitro photothermal ablation of 4T1 cells

The 4T1 cells were seeded into 96-well plates and incubated for 24 h to allow the cells to be attached. Then, the medium was carefully removed and fresh medium containing the same PcRu concentration (20 μM) of PcRu-NP or α-PcRu-NP was added to each well. After incubation for 4 h, the cells were washed to remove non-internalized NPs and irradiated with a 670 nm laser (0.5 W/cm^2) for 10 min. Then, the cells were incubated for an extra 20 h, and cell viability was measured *via* the MTS assay according to the procedure described above.

2.13. Mouse tumor models establishment

Female BALB/c mice (6–7 weeks old) were purchased from Hunan SJA Laboratory Animal Co. Ltd. (Changsha, Hunan, China). All animal studies were performed in compliance with the protocols approved by the Hubei Provincial Animal Care and Use Committee (2019S2044) and were conducted with the experimental guidelines of the Animal Experimentation Ethics Committee of the Huazhong University of Science and Technology. A total of 1 × 10^6 4T1 cells were subcutaneously implanted into the right flanks of the mice to develop the subcutaneous tumor-bearing model.

2.14. In vivo optoacoustic imaging

Tumors were allowed to grow to a volume of approximately 100 mm^3. The α-PcRu-NP or PcRu-NP (PcRu concentration: 180 μM/200 μL) were intravenously injected into 4T1 tumor-bearing mice. Then, the imaging target (tumor) was well mounted in the protruding top of the bowl. The image position was consistent to facilitate comparisons. Finally, optoacoustic imaging of the image target was acquired according to different injection times. Pre-injection scans were used as controls.

2.15. In vivo photothermal imaging

When 4T1 cell tumor reached an average volume of ∼ 100 mm^3, α-PcRu-NP or PcRu-NP (PcRu concentration: 180 μM/200 μL) was intravenously injected into the mice. Mice intravenously injected with PBS were used as a control. After 12 h, the tumor site was exposed to a 670 nm laser with an output power density of 0.5 W/cm^2 for 5 min. During the process of laser radiation, temperature and whole-body infrared images were captured by a thermal imaging camera (VaricCAM, Germany) at different time points.

2.16. Mouse tumor models and treatment

When the tumor volume reached 100 mm^3, the mice were divided into six groups (n = 4) and intratumoral injected with different nanoparticles: (I) PBS, (II) Laser, (III) PcRu-NP, (IV) α-PcRu-NP, (V) PcRu-NP + laser, and (VI) α-PcRu-NP + laser (concentration of PcRu: 180 μM/200 μL). During the therapeutic period, each mouse's body weight and tumor volumes were recorded, and the volume was calculated according to the following formula: V (mm^3) = L × W^2/2, where L represents the longest dimension and W represents the perpendicular dimension to L.

For biochemical and histopathological analysis, the blood of the mice was collected for the further detection of alanine aminotransferase (ALT), aspartate aminotransferase (AST), blood urea nitrogen (BUN), creatinine (CREA), total bilirubin (T-BIL), and urea (UA). The major organs (heart, liver, spleen, lung, kidney) were harvested and fixed in 4 % paraformaldehyde solution for H&E staining.

For detection of apoptotic tumor cells, tumors were collected on 3rd day after various treatments, and the tumors were fixed in 4 %

paraformaldehyde solution for hematoxylin/eosin (H&E) and immunofluorescence staining with the TUNEL assay kit (TUNEL, Beyotime).

2.17. In vivo anti-tumor immune response analysis by immunofluorescence assay and flow cytometry

The mice were sacrificed on the 3rd day after drug treatment, and the tumors were harvested for analysis of immune responses. For the immunofluorescence analysis, tumor tissues were immunostained with anti-CD206-AF647 (Biolegend, Clone C068C2), anti-CD11c-APCcy7 (Biolegend, Clone HL3), anti-CD8-AF647 (Biolegend, Clone 53–6.7) and PI. For flow cytometry analysis, the tumors were digested with a high-activity tumor tissue enzymatic digestion kit (RED, DHTE-5001). The digested tumors were filtered with a 70 μm cell strainer to generate single-cell suspensions. For macrophage analysis, the cells were stained with Zoombie-NIR™, anti-CD45-FITC (Biolegend, Clone S18009F), anti-CD11b-PE/Cy7 (Biolegend, Clone M1/70), anti-F4/80-AF647 (Biolegend, Clone BM8), anti-CD86-PE (Biolegend, Clone A17199A), anti-CD206-BV421 (Biolegend, Clone C068C2). For DCs analysis, the cells were stained with Zoombie-NIR™, anti-CD45-PE (Biolegend, Clone I3/2.3), anti-CD11c-FITC (Biolegend, Clone N418), anti-CD80-BV510 (Biolegend, Clone 16-10A1), anti-CD86-BV421 (Biolegend, Clone GL-1), and anti-MHCII-PE/Cy7 (Biolegend, Clone M5/114.15.2). For IFN-γ analysis, the cells were stained with Zoombie-NIR™, anti-CD45-FITC (Biolegend, Clone S18009F), anti-CD3-Percp5.5 (Biolegend, Clone 17A2), anti-CD4-PE/Cy7 (Biolegend, Clone GK1.5), anti-CD8-BV421 (Biolegend, Clone 53–6.7), anti-IFN-γ-PE (Biolegend, Clone XMG1.2). Antibody staining was conducted according to the manufacturer's instructions. Cells were analyzed on a CytoFLEX S flow cytometry (Beckman, USA), and data were analyzed with FlowJo software.

2.18. Statistical analysis

Statistical analysis was performed using GraphPad Prism (GraphPad Software, Inc., La Jolla, CA, USA). For the comparison of three or more groups, one-way ANOVA with Tukey's multiple compassion test was performed. For comparisons of the two groups, a two-tailed unpaired *t*-test was performed. All statistical data are expressed as the mean ± SD. Significant differences between the groups were labeled n.s. for not significant values, or * for $p < 0.05$, ** for $p < 0.01$, *** for $p < 0.001$, and **** for $p < 0.0001$.

3. Results and discussion

3.1. Synthesis and characterization of PcRu

Chromophores with *J*-type aggregation are promising candidates for biological/biomedical applications with enhanced laser absorption and photodynamic efficiency. Due to the rigid structure which restricts the formation of the required face-to-face stacking, the *J*-type aggregation in phthalocyanines is not as common as in other chromophores [29]. Considering its symmetric molecular structure and potential π-π stacking originating from the multiple aromatic rings, the structure of Pcs was designed and symmetrically modified with minimized steric hindrance. The introduction of benzodioxin, an electron-donating substituent on the periphery of the phthalocyanine ring, and the involvement of ruthenium, a six-coordinate transition metal, were employed to realize this. The synthesis route was presented in Scheme S1. The final compound PcRu was prepared in moderate yield by refluxing phthalonitrile compound and triruthenium dodecacarbonyl ($Ru_3(CO)_{12}$), in the presence of 1,8-diazabicyclo[5.4.0]undec-7-ene (DBU). After purification by silica gel column chromatography, the dark green product was obtained. The synthesized PcRu was characterized by IR and high-resolution mass spectrometry. The IR absorption bands of major functional groups such as -NH, -N=C, -C=C, −1,2-substituted benzene appeared in the IR spectrum (Fig. S1). The CO was automatically coordinated in the axial direction of PcRu and its molecular ion peak was found to be: 1518.45 (calculated: 1518.27). The UV–vis absorption of PcRu in DMSO was depicted in Fig. S2. The absorption maximum of PcRu was located at 730 nm ($\varepsilon = 8.6 \times 10^4\ M^{-1}cm^{-1}$), with an obvious bathochromic shift compared to Pcs (70 nm). This can be explained by the elongation of the conjugated π structure with benzodioxin in the periphery of the Pc ring.

3.2. Preparation and characterization of α-PcRu-NPs

To improve the stability and targeting ability for the *in vivo* applications, the small molecule PcRu was encapsulated into lipid nanoparticles with M2 mimetic peptide modification, termed α-PcRu-NPs (Fig. 1a). It was detected by the UV–vis that the loading efficiency of PcRu in α-PcRu-NPs was 70.4 ± 0.5 %. The α-PcRu-NPs displayed uniform spherical morphology with a larger size than PcRu-NPs (23.2 ± 1.2 nm *vs.* 22.4 ± 1.1 nm, Fig. 1b and S3), suggesting the successful coating M2 mimetic peptide on the lipid nanoparticles. Besides, the spectra demonstrated that the α-PcRu-NPs had a slight bathochromic shift to 740 nm compared with PcRu small molecule and a moderate extinction coefficient ($\varepsilon = 2.4 \times 10^4\ M^{-1}cm^{-1}$), which may be explained by the formation of *J*-type aggregation of PcRu in core of nanoformulations. When 1 % triton X-100 was added to α-PcRu-NPs, the PcRu was released from the intact structure and the maximum absorbance returned to 730 nm (Fig. 1c). The measured zeta potential of α-PcRu-NPs was 2.42 ± 0.52 mV (Table S1). It was noteworthy that only 20 % of the total PcRu was released from α-PcRu-NPs during 48 h of incubation in 37 °C PBS solution, suggesting that α-PcRu-NPs maintain high stability in blood circulation and *in vivo* experiments (Fig. S4).

Next, the photophysical and photochemical properties of α-PcRu-NPs and PcRu were evaluated. The fluorescence of α-PcRu-NPs and PcRu was completely quenched compared to DiR-BOA (a NIR fluorescence dye), due to the introduction of transition-metal Ru (Fig. 1d). Additionally, the $^1O_2$ production efficiency of α-PcRu-NPs was decreased by 73 % than PcRu based on the decay rate of 1,3-diphenylisobenzofuran (DPBF) (Fig. 1e). Besides, whether α-PcRu-NPs can produce other types of ROS was investigated. As shown in Fig. S5, few fluorescence changes of APF (•OH indicator) or DHR 123 ($\cdot O_2^-$ indicator) were observed after photoinduction of α-PcRu-NPs, indicating α-PcRu-NPs have no •OH/$\cdot O_2^-$ generation capacities. The weak fluorescence emission and reduced singlet oxygen generation probably indicated the α-PcRu-NPs have a high potential as a PAI and PTT agent. As shown in Fig. 1f, α-PcRu-NPs induced stronger PA amplitude with 7.2-fold higher than that of PcRu, suggesting the aggregation state formation in the α-PcRu-NPs. Meanwhile, α-PcRu-NPs showed a high photothermal effect due to their strong PA amplitude. After irradiation with 670 nm laser at 0.5 W/cm^2 for 5 min, the temperature of α-PcRu-NPs (20 μM) increased from 27 to 35 °C. However, under the same conditions, the temperature of PcRu only increase to 31 °C (Fig. 1g). In addition, α-PcRu-NPs exhibited the ability to raise the temperature quickly by increasing the PcRu concentration of nanoparticles or increasing laser power (Fig. S6). The PCE of α-PcRu-NPs can reach approximately 60 % (Fig. 1h), which is higher than that of previously reported Pc-based nanocomposites, such as ZnPc NP (31.3 %) [36], Bio-ZnPc-Pdot (38.17 %) [37], and comparable to Zn4-H2Pc/DP NP (58.3 %) [38]. These results indicated that α-PcRu-NPs may effectively convert light to heat and are likely to be a promising contrast agent for PA imaging and PTT.

The photophysical processes of α-PcRu-NPs as PAI/PTT agent were depicted in Fig. 1i. After photoexcitation of PcRu, electrons are excited from the singlet ground state (S_0) to the excited singlet state (S_1) with a higher energy. Subsequently, excited S_1 drives back to the S_0 through three main competitive processes: emission photos (i.e., fluorescence), intersystem crossing (ISC, which mostly contributes to the generation of reactive oxygen species), and vibrational relaxation (thermal release). Normally, the fluorescence of PcRu was negligible owing to transition metals [39]. When PcRu was present as a single molecule, the ISC decay

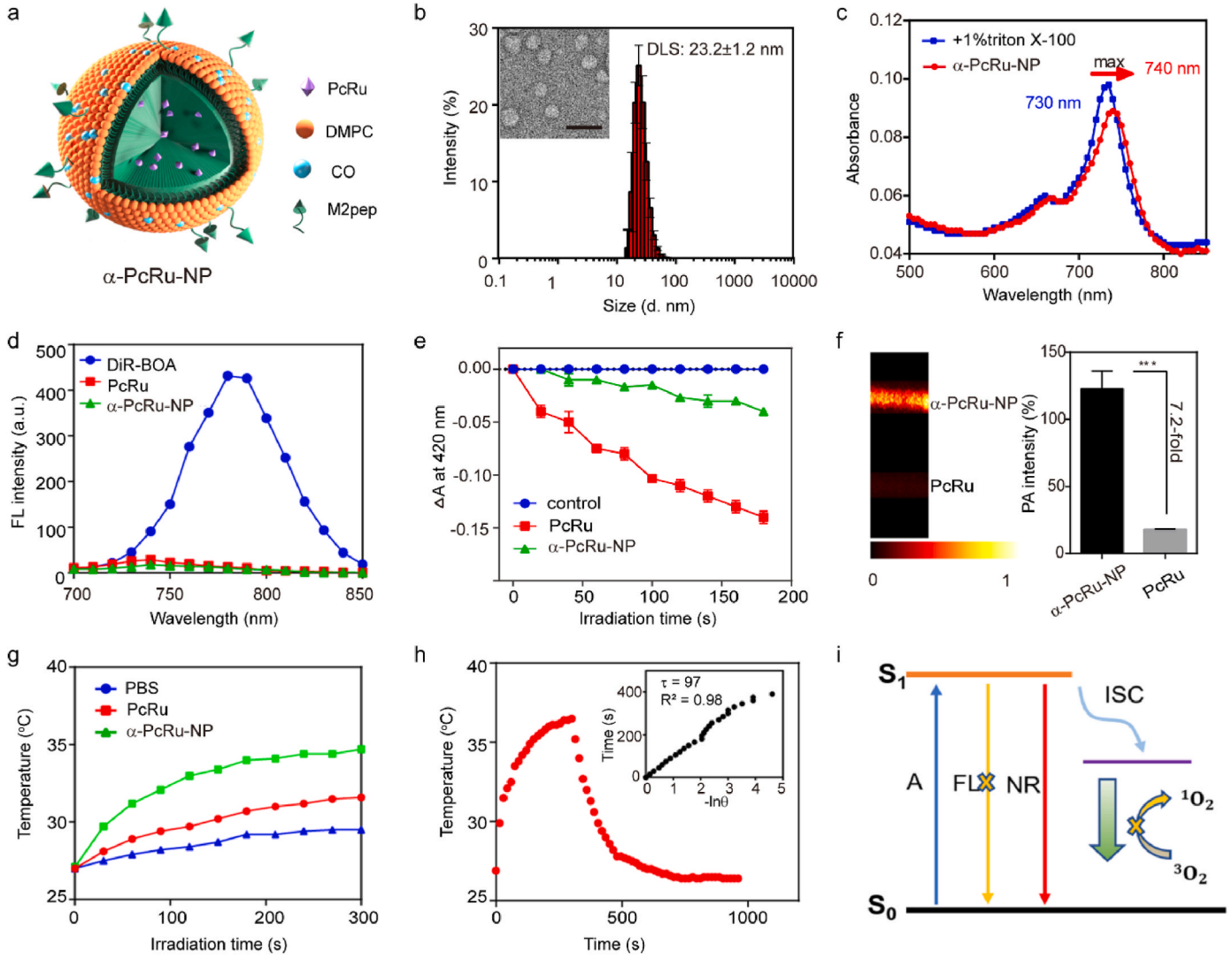

Fig. 1. Preparation and characterization of α-PcRu-NPs. (a) Schematic diagrams of α-PcRu-NPs. (b) The DLS profile and TEM graph of α-PcRu-NPs (scale bar: 50 nm). (c) The UV–vis absorption spectra of α-PcRu-NPs and disrupted α-PcRu-NPs by adding 1 % triton X-100. (d) The fluorescence spectra of α-PcRu-NPs, PcRu, and DiR-BOA at the same concentration (PcRu concentration: 10 μM; DiR-BOA concentration: 10 μM). (e) Photodegradation rate of DPBF. (f) Photoacoustic images and quantitative results of tube containing α-PcRu-NPs and PcRu. (g) Temperature variation curves of α-PcRu-NPs and PcRu (20 μM) solution irradiated by 670 nm laser (0.5 W/cm^2). (h) Temperature changes of α-PcRu-NPs with/without 670 nm laser irradiation and photothermal conversion efficiency. (i) Simplified Jablonski diagram of α-PcRu-NPs, in which the ROS decay is minimized, thus the excited state is retained for improving the nonradiative decay pathway.

pathway predominated and led to substantial singlet oxygen quantum yields ($\varnothing_\Delta$ = 0.80–0.99) [40]. While in α-PcRu-NPs, the ISC decay process was inhibited, which may contributed to the formation of *J*-type aggregation of PcRu in the centre of the nanostructure. Thus α-PcRu-NPs could function as photoacoustic agents since the nonradiative (NR) decay pathway being dominant.

3.3. M2 macrophage and 4T1 tumor efficient targeting

To investigate the M2-like macrophage targeting ability of α-PcRu-NPs, IL-4 stimulated RAW264.7 cells were co-incubated with DiR-BOA (a fluorescent dye)-loaded nanoparticles (α-PcRu-NPs(DiR-BOA) and PcRu-NPs(DiR-BOA)) for different incubation time. As shown in Fig. 2a, M2-like macrophage exhibited a stronger intracellular red fluorescence in α-PcRu-NPs(DiR-BOA)-treated group than PcRu-NPs(DiR-BOA)-treated group after incubation for 3 h, suggesting a preferable M2-like macrophage targeting capacity of α-PcRu-NPs. Meanwhile, the uptake efficiency of nanoparticles by M2 macrophage was quantified by using flow cytometry (Fig. 2b and S7). The results revealed that M2 macrophages acquired significantly more α-PcRu-NPs than PcRu-NPs in a time-dependent manner (9.9-fold at 1 h, 16.5-fold at 3 h, and 17.5-fold at 6 h, NPs contained with the same DiR-BOA concentration (1 μM), respectively). Meanwhile, the uptake efficiency of NPs by 4T1 tumor cells were represented in Fig. 2c. The α-PcRu-NPs (DiR-BOA: 1 μM) captured by 4T1 cells were also higher than PcRu-NPs with 8.36-fold at 1 h, 11.6-fold at 3 h, and 15.5-fold at 6 h, respectively. These results indicate that α-PcRu-NPs with M2pep peptide modification can efficiently target both M2 macrophages and 4T1 tumor cells.

Encouraged by the high PCE of α-PcRu-NPs, *in vitro* PTT efficacy of α-PcRu-NPs was evaluated by the MTS assay (Fig. 2d). After incubating 4T1 cells with varying concentrations of NPs (PcRu concentration: 0, 5, 10, 20 μM) in the dark, α-PcRu-NPs demonstrated minimal dark cytotoxicity and high survival rates (~ 100 %), manifesting the low cytotoxicity of ruthenium complexes [41]. After exposure to the 670 nm laser (0.5 W/cm^2) for 5 min, a notable concentration-dependent photocytotoxicity was observed, with an IC_{50} of 20 μM. Next, different nanoparticles were incubated with 4T1 cells either with or without 670 nm laser irradiation (Fig. 2e). After irradiation with 670 nm laser (0.5

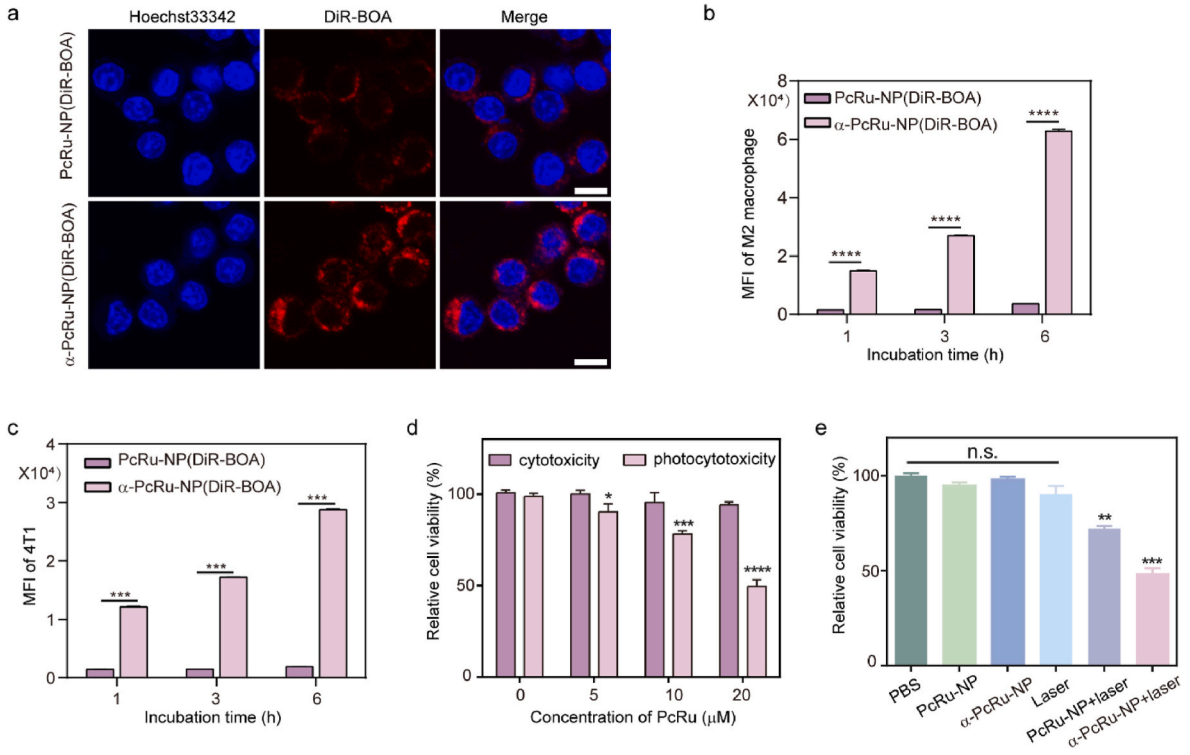

Fig. 2. *In vitro* M2-like macrophage and 4T1 targeting ability and photothermal efficiency of α-PcRu-NPs. (a) Confocal imaging of α-PcRu-NPs and PcRu-NPs co-cultured with M2-like macrophage. Scale bar: 10 μm. (b) MFI of DiR-BOA (1 μM) in M2-like macrophages at different incubation times. (c) MFI of DiR-BOA (1 μM) in 4T1 at different incubation times. (d) MTS assay of 4T1 cells incubated with different concentrations of α-PcRu-NPs with or without 670 nm laser irradiation (0.5 W/cm^2, 5min). (e) Assessment of the *in vitro* photothermal therapy effect with various treatments.

W/cm^2) for 5 min, the PcRu-NPs+laser group exhibited photocytotoxicity with 69 % cell viability, but the α-PcRu-NPs+laser group significantly increased photocytotoxicity, leading to the survival rate of 4T1 cells being about 50 %. PcRu-NP- and α-PcRu-NP-treated group did not exhibit obvious toxicity. Owing to the targeting capability, the increased cellular uptake of α-PcRu-NPs by 4T1 cells resulted in an augmented photocytotoxicity of PTT, which suggested α-PcRu-NPs could be a prominent PTT agent for tumor treatment *in vivo*.

3.4. In vivo photoacoustic imaging

Subsequently, whether α-PcRu-NPs could be used for *in vivo* PA imaging was assessed. An acoustic-resolution photoacoustic microscopy (AR-PAM) system with high resolution (45–50 μm) and a millimeter-sized scan range established in our lab was utilized to obtain 744 nm signal images in previous studies [42,43]. The α-PcRu-NPs and PcRu-NPs (concentration of PcRu: 180 μM/200 μL) were intravenously injected into Balb/c mice bearing with 4T1 tumor, and their PA signal was imaged at various intervals after the injection. For α-PcRu-NP--treated group, the PA signals of the XY-axis planer were gradually enhanced (Fig. 3a up), and Z-axis depth information (Fig. 3a down) became more fruitful over time and reached a peak at 12 h postinjection. In contrast, PA signals in the PcRu-NP-treated group remained consistently weak and only distributed in the peripheral and superficial regions of the tumor (Fig. 3b). Quantitative analysis also revealed that average PA intensity in the α-PcRu-NP-injected group was considerably higher than that of the PcRu-NP-injected group over time, reaching up to 2.75-fold higher at 12 h postinjection (Fig. 3c). The mice treated with α-PcRu-NPs exhibited noteworthy PA signals, indicating that the small size and tumor-targeting effect of α-PcRu-NPs enable efficient tumor accumulation.

Meanwhile, the intensity of the photoacoustic signal was plotted along the intratumoral blood vessels (white line in Fig. 3a and b). The endogenous molecules (e.g., hemoglobin) were used to characterize the blood vessel (Fig. S8). The peak intensity of α-PcRu-NPs was approximately 2.5-fold higher than that of PcRu-NPs in blood vessels of tumors (Fig. 3d), suggesting that α-PcRu-NPs might be able to reach the interior of solid tumors *via* the blood vessel efficiently. More importantly, the 3D reconstruction (Fig. 3e) and selected cross-section slides (Figs. S9 and S10) of the PA signal in the tumor region also intuitively revealed the intratumor accumulation of α-PcRu-NPs in detail, which is a powerful tool to optimize the invention time of PTT personality and visualize treatment results in time. The statistical results depicted in Fig. 3f also illustrated that the intratumor distribution of α-PcRu-NPs was deeper than that of PcRu-NPs. These results presented that the penetration of α-PcRu-NPs was deeper than PcRu-NPs, which might be attributed to the targeting peptide modification and small size. The PA signal in blood was detected to assess the blood circulation of NPs. The results also demonstrated that the α-PcRu-NPs could maintain blood circulation for 12 h, allowing the nanoparticles to efficiently accumulate in the tumor for PA imaging and PTT (Fig. 3g). All results confirmed that α-PcRu-NPs could efficiently target and distribute into the interior of solid tumors, indicating that α-PcRu-NPs should be a promising phototherapeutic agent for PAI-guided PTT.

3.5. In vivo PTT efficacy

To investigate whether α-PcRu-NP with laser could trigger an efficient anti-tumor effect in breast cancer, nanoparticles were intravenously injected into 4T1 tumor-bearing mice and the treatment process was represented in Fig. 4a. The tumor-bearing mice were randomly divided into 6 groups: PBS, laser, PcRu-NP, α-PcRu-NP, PcRu-NP+laser, and α-PcRu-NP+laser (concentration of PcRu: 180 μM/200 μL) when the tumor volume reached 100 mm^3. For mild photothermal therapy, multiple short-term laser irradiation was used, heating the tumor for 3 min each time with the laser irradiation (670 nm, 0.5 W/cm^2) at 12 h, 15 h

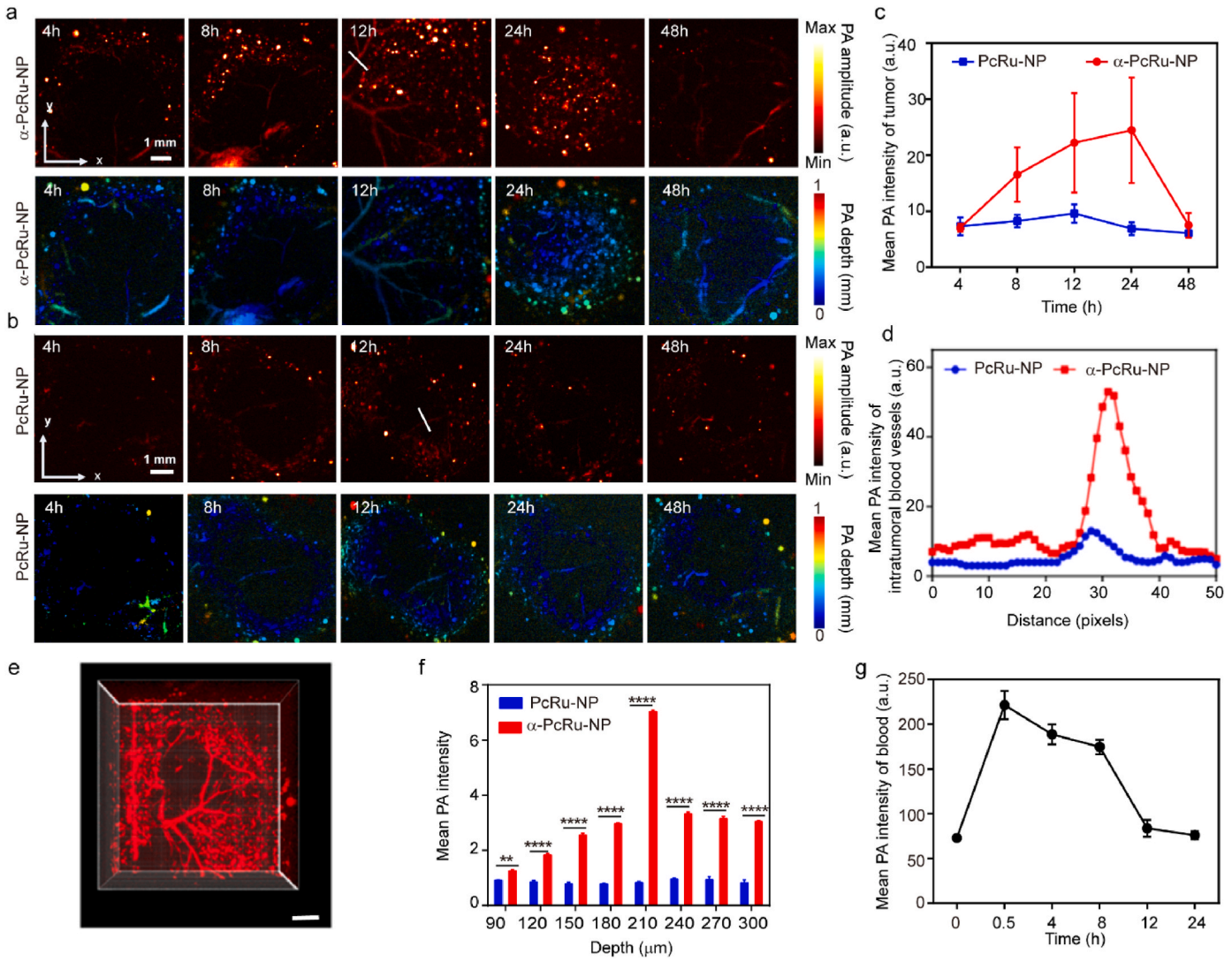

Fig. 3. *In vivo* PA imaging of 4T1-bearing mice after intravenous injection of α-PcRu-NPs. (a–b) *In vivo* PA images of the tumor region (up) and depth along the Z-axis (down) at 4, 8, 12, 24, and 48 h after intravenous injection of (a) α-PcRu-NPs and (b) PcRu-NPs. (c) Quantitative outcomes of the inner tumor PA signal changes at different time points after the injection of α-PcRu-NPs and PcRu-NPs. (d) Photoacoustic signal intensity plot of intratumoral blood vessels after 12 h postinjection (marked with white lines). (e) 3D reconstruction of 4T1 tumor with α-PcRu-NPs postinjection. Scale bar: 1000 μm. (f) The PA intensity of PcRu-NPs and α-PcRu-NPs at the different depths. (g) Quantitative data of blood PA signal changes at various intervals after α-PcRu-NPs injection. Data are presented as the mean ± SD, n = 3 mice/group (two-tailed).

and 18 h postinjection of various drugs. The temperature variations under laser irradiation were tracked using an IR thermal camera (Fig. 4b and c). After 12 h postinjection, the tumor was exposed to a 670 nm laser at a power density of 0.5 W/cm^2 for 5 min. With the injection of the α-PcRu-NPs, the temperature of the tumor region showed a rapid increase (from 31.2 °C to 59.6 °C after 60 s and finally stabilizes at 73 °C), whereas a steady increase of temperature (from 31 °C to 56.6 °C in 5 min) was observed in PcRu-NPs-treated group. The control group exhibited a slight change in temperature (less than 15 °C) of tumor under the same conditions. These results indicate that the α-PcRu-NPs have great potential to be an effective PTT agent for the treatment of solid tumors *in vivo*. The *ex vivo* images of the tumor on the 15th day (Fig. 4d) and tumor growth curve (Fig. 4e) showed that α-PcRu-NP with laser dramatically inhibits tumor growth. Compared with the tumor volume of the PBS group (1002 mm^3), mice treated with laser (960 mm^3), PcRu-NP (819 mm^3) and α-PcRu-NP (775 mm^3) exhibited little anti-tumor effect. Especially, mice treated with PcRu-NP+laser and α-PcRu-NP+laser were able to inhibit tumor growth, and the α-PcRu-NP+laser group (12 mm^3) showed more excellent ability to eliminate the tumor than the PcRu-NP+laser group (49 mm^3). The body weight of mice showed no abnormality (Fig. 4f).

Furthermore, the TUNEL analysis of tumor tissue also suggested that α-PcRu-NP induced the strongest apoptosis of tumors with laser (Fig. 4g). The biochemical markers of blood serum (Fig. S11) and H&E staining of major organs (Fig. S12) were measured to study the biosafety of α-PcRu-NP. No noticeable hepatic or renal dysfunction and no obvious organ damage were observed for all treatment groups. These data suggest that α-PcRu-NP is a biocompatible nanomedicine and could enhance the PTT efficacy.

3.6. Immune response in vivo

Modulating the tumor immune microenvironment is an effective strategy to promote anti-tumor treatment. Photothermal therapy has been reported to trigger the immunogenic cell death of tumors, following dendritic cell (DCs) maturation, cytotoxic T cell infiltration, and tumor microenvironment regulation. To verify the underlying mechanism of the nanomedicine-based immune response, we evaluated

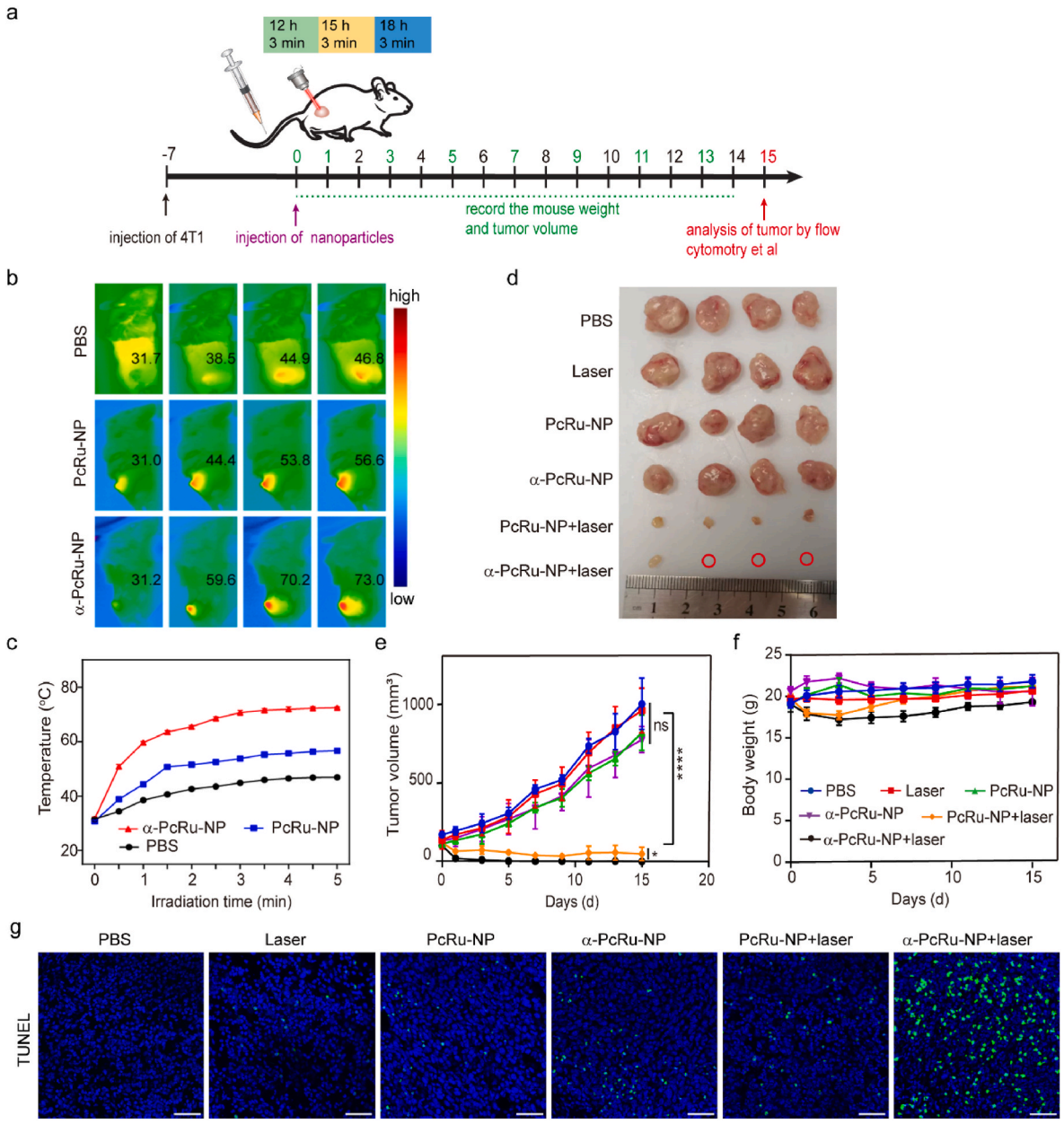

Fig. 4. *In vivo* evaluations of the photothermal anti-tumor effect of α-PcRu-NP on breast cancer. (a) Experimental timeline of the treatment of 4T1-bearing mice. (b) Thermal IR images of mice bearing 4T1 tumors. (c) Temperature change curves of 4T1 tumors in mice receiving the prescribed treatments. Data are presented as the mean ± SD, n = 3 (two tails). (d) The photograph of tumors from each group on the 15th day. (e) Tumor growth curves of 4T1 tumors in each group after different treatments (n = 4). (f) Body weight changes of mice in the period of treatment. (g) Tumor tissue TUNEL staining analysis after various treatments. Scale bar: 50 μm.

the tumor microenvironment involving M2 macrophage, DCs, cytotoxic T cells, etc. The flow cytometry gate strategies of different cells were shown in Fig. S13. As shown in Fig. 5a, compared with the PBS group (60 %), the α-PcRu-NP+laser-treated group significantly decreased the proportion of M2-like macrophage ($CD206^+$) to 38 %, modulating the tumor immunosuppressive microenvironment in tumors. In addition, the percentage of mature DCs ($CD80^+CD86^+$) in α-PcRu-NP+laser group increased to 35 %, which was approximately 1.3 times higher than those in the PBS group (28 %, Fig. 5b). More IFN-γ^+ $CD8^+$ T cells (2.1-fold higher than in the PBS group) were found in the group of α-PcRu-NP+laser (Fig. 5c). The performance of immunofluorescence also confirmed the efficient anti-tumor immune efficacy of the α-PcRu-NP+laser group (Fig. 5d). In results, α-PcRu-NP with laser irradiation can not only effectively modulate immunosuppressive microenvironment, but also promote anti-tumor immune response.

Phthalocyanine molecules were firstly developed with the *J*-type aggregation capability as confirmed by the red-shift absorption. Meanwhile, the internal coordination of ruthenium resulted in the effective suppression of fluorescence emission and improves the photothermal conversion efficiency. Loaded in liposome nanoparticles modified with M2 targeting peptides, the photothermal conversion efficiency of the novel developed PcRu can be further improved. By utilizing this targeted nanocarrier, it was able to achieve efficient accumulation and depth PA imaging of the tumor interior. Besides, PTT with α-PcRu-NPs contributed to the effective suppression or elimination of tumors. Such a novel photothermal reagent is expected to provide a useful tool for clinical tumor treatment.

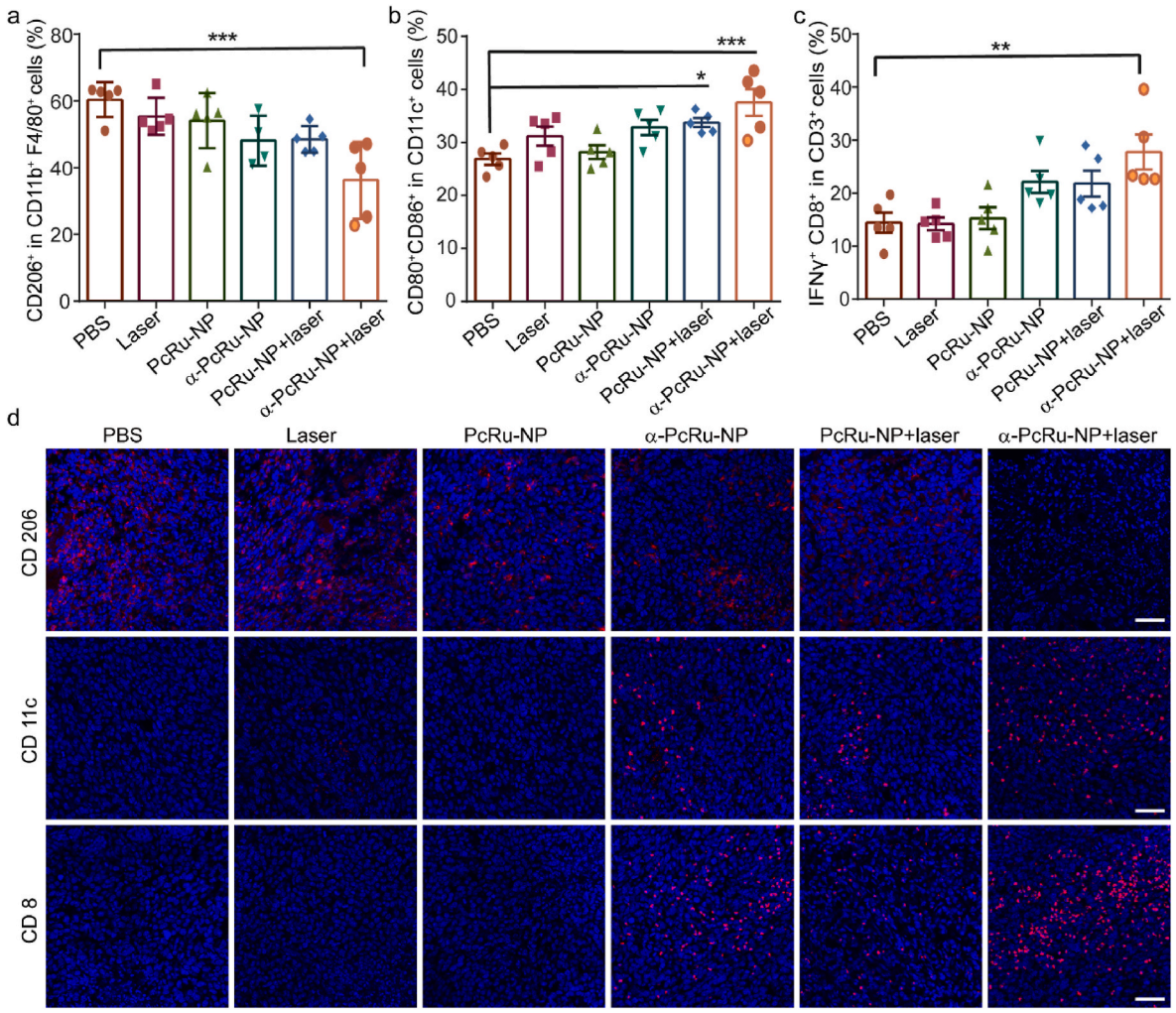

Fig. 5. *In vivo* immune response of α-PcRu-NP in 4T1-bearing mice. (a–c) Percentages of proliferated M2 cells (a), DCs (b), and IFN- γ^+ $CD8^+$ T cells (c). (d) Immunofluorescence staining of CD206, CD11c and $CD8^+$ T cells. Scale bar: 50 μm.

4. Conclusions

In summary, a NIR laser activated ruthenium phthalocyanine-loaded lipid nanoparticles (α-PcRu-NPs) with M2 macrophage targeting was developed and employed as a phototheranostic agent for PAI-guided PTT. Take advantages of PcRu small molecule with *J*-type aggregation in nanostructure, α-PcRu-NPs exhibits efficient NIR absorption, reduced singlet oxygen generation, excellent photothermal activity, and high contrast of photoacoustic imaging with a high PCE of 60 % *in vitro*. Due to small size and M2pep modification of nanocarrier, α-PcRu-NPs can effectively visualize the tumor with high contrast PA imaging and facilitate light-induced thermal ablation of the tumor *in vivo*. Furthermore, α-PcRu-NPs with laser can trigger the tumor immune response, decrease M2 macrophage, promote the maturation of DCs and infiltrate cytotoxic T cells in tumors. By developing the PAI/PTT applications for PcRu, our work paves the way for future explorations into clinical and nanomedicine applications of this multifunctional phototheranostic agent in future.

CRediT authorship contribution statement

Xingzhou Peng: Writing – original draft, Visualization, Supervision, Methodology, Investigation, Funding acquisition, Data curation, Conceptualization. **Junjie Wang:** Writing – original draft, Investigation, Funding acquisition, Data curation, Conceptualization. **Zihan Deng:** Writing – original draft, Methodology, Investigation, Data curation. **Jianshuang Wei:** Methodology, Investigation, Data curation. **Changqiang Xie:** Investigation. **Yan Wang:** Investigation, Data curation. **Jianlei Han:** Methodology, Investigation, Data curation. **Zhengyu Chen:** Investigation. **Jianghai Du:** Investigation. **Zhihong Zhang:** Writing – review & editing, Supervision, Project administration, Funding acquisition, Conceptualization.

Declaration of competing interest

The authors declare that they have no known competing financial interests or personal relationships that could have appeared to influence the work reported in this paper.

Data availability

Data will be made available on request.

Acknowledgments

This research was supported by the Science and Technology Talent Innovation Project in Hainan Province (KJRC2023B09), the Innovation Fund of WNLO, the Hainan Provincial Natural Science Foundation of China (823RC472), the Education Department of Hainan Province (Hnky2024ZD-12), and the Open Project Program of Wuhan National

Laboratory for Optoelectronics (2021WNLOKF008). We also thank the Optical Bioimaging Core Facility of WNLO-HUST and the Research Core Facilities for Life Science (HUST) for the support in data acquisition, and the Analytical & Testing Center of HUST for spectral measurements.

Appendix A. Supplementary data

Supplementary data to this article can be found online at https://doi.org/10.1016/j.mtbio.2024.101209.

References

[1] C. Xia, X. Dong, H. Li, M. Cao, D. Sun, S. He, F. Yang, X. Yan, S. Zhang, N. Li, W. Chen, Cancer statistics in China and United States, 2022: profiles, trends, and determinants, Chin. Med. J. 135 (5) (2022) 584–590.
[2] R.K. Pachynski, E.H. Kim, N. Miheecheva, N. Kotlov, A. Ramachandran, E. Postovalova, I. Galkin, V. Svekolkin, Y. Lyu, Q. Zou, D. Cao, J. Gaut, J. E. Ippolito, A. Bagaev, M. Bruttan, O. Gancharova, K. Nomie, M. Tsiper, G. L. Andriole, R. Ataullakhanov, J.J. Hsieh, Single-cell spatial proteomic revelations on the multiparametric MRI heterogeneity of clinically significant prostate cancer, Clin. Cancer Res. 27 (12) (2021) 3478–3490.
[3] P. Liang, B. Ballou, X. Lv, W. Si, M.P. Bruchez, W. Huang, X. Dong, Monotherapy and combination therapy using anti-angiogenic nanoagents to fight cancer, Adv. Mater. 33 (15) (2021) 2005155.
[4] Y. Yin, X. Ge, J. Ouyang, N. Na, Tumor-activated in situ synthesis of single-atom catalysts for O_2-independent photodynamic therapy based on water-splitting, Nat. Commun. 15 (1) (2024) 2954.
[5] C. Wang, W. Fan, Z. Zhang, Y. Wen, L. Xiong, X. Chen, Advanced nanotechnology leading the way to multimodal imaging-guided precision surgical therapy, Adv. Mater. 31 (49) (2019) 1904329.
[6] M. Gerlinger, Targeted drugs ramp up cancer mutability, Science 366 (6472) (2019) 1452–1453.
[7] X. Li, W. Song, C. Shao, Y. Shi, W. Han, Emerging predictors of the response to the blockade of immune checkpoints in cancer therapy, Cell. Mol. Immunol. 16 (1) (2019) 28–39.
[8] W. Zou, Immune regulation in the tumor microenvironment and its relevance in cancer therapy, Cell. Mol. Immunol. 19 (1) (2022) 1–2.
[9] J.W. Bai, S.Q. Qiu, G.J. Zhang, Molecular and functional imaging in cancer-targeted therapy: current applications and future directions, Signal Transduct. Targeted Ther. 8 (1) (2023) 89.
[10] X. Bao, Y. Yuan, J. Chen, B. Zhang, D. Li, D. Zhou, P. Jing, G. Xu, Y. Wang, K. Hola, D. Shen, C. Wu, L. Song, C. Liu, R. Zboril, S. Qu, In vivo theranostics with near-infrared-emitting carbon dots-highly efficient photothermal therapy based on passive targeting after intravenous administration, Light Sci. Appl. 7 (2018) 91.
[11] P. Thi Tuong Vy, B. Nhat Quang, S.W. Cho, S. Bharathiraja, P. Manivasagan, M. S. Moorthy, S. Mondal, C.S. Kim, J. Oh, Photoacoustic imaging-guided photothermal therapy with tumor-targeting HA-FeOOH@ PPy nanorods, Sci. Rep. 8 (1) (2018) 8809.
[12] Y. Zhang, J. Olick Gibson, A. Khadria, L.V. Wang, Photoacoustic vector tomography for deep haemodynamic imaging, Nat. Biomed. Eng. 8 (2024) 701–711.
[13] I. Fernández Ruiz, Photoacoustic method enables deep imaging of blood flow, Nat. Rev. Cardiol. 21 (2) (2024), 72-72.
[14] Q. Fu, R. Zhu, J. Song, H. Yang, X. Chen, Photoacoustic imaging: contrast agents and their biomedical applications, Adv. Mater. 31 (6) (2019) 1805875.
[15] Y. Han, Y. An, G. Jia, X. Wang, C. He, Y. Ding, Q. Tang, Theranostic micelles based on upconversion nanoparticles for dual-modality imaging and photodynamic therapy in hepatocellular carcinoma, Nanoscale 10 (14) (2018) 6511–6523.
[16] G. Wen, X. Li, Y. Zhang, X. Han, X. Xu, C. Liu, K.W.Y. Chan, C.S. Lee, C. Yin, L. Bian, L. Wang, Effective phototheranostics of brain tumor assisted by near-infrared-II light-responsive semiconducting polymer nanoparticles, ACS Appl. Mater. Interfaces 12 (30) (2020) 33492–33499.
[17] B. Li, W. Wang, L. Zhao, Y. Wu, X. Li, D. Yan, Q. Gao, Y. Yan, J. Zhang, Y. Feng, J. Zheng, B. Shu, J. Wang, H. Wang, L. He, Y. Zhang, M. Pan, D. Wang, B.Z. Tang, Y. Liao, Photothermal therapy of tuberculosis using targeting pre-activated macrophage membrane-coated nanoparticles, Nat. Nanotechnol. 19 (2024) 834–845.
[18] Z. Shi, M. Luo, Q. Huang, C. Ding, W. Wang, Y. Wu, J. Luo, C. Lin, T. Chen, X. Zeng, L. Mei, Y. Zhao, H. Chen, NIR-dye bridged human serum albumin reassemblies for effective photothermal therapy of tumor, Nat. Commun. 14 (1) (2023) 6567.
[19] M. Shi, Z. Fu, W. Pan, Y. Chen, K. Wang, P. Zhou, N. Li, B. Tang, A protein-binding molecular photothermal agent for tumor ablation, Angew. Chem. Int. Ed. 60 (24) (2021) 13564–13568.
[20] H. Wang, J. Chang, M. Shi, W. Pan, N. Li, B. Tang, A dual-targeted organic photothermal agent for enhanced photothermal therapy, Angew. Chem. Int. Ed. 58 (4) (2019) 1057–1061.
[21] W.S. Chan, J.F. Marshall, R. Svensen, J. Bedwell, I.R. Hart, Effect of sulfonation on the cell and tissue distribution of the photosensitizer aluminum phthalocyanine, Cancer Res. 50 (15) (1990) 4533–4538.
[22] X. Li, B.D. Zheng, X.H. Peng, S.Z. Li, J.W. Ying, Y. Zhao, J.D. Huang, J. Yoon, Phthalocyanines as medicinal photosensitizers: developments in the last five years, Coord. Chem. Rev. 379 (2019) 147–160.
[23] P.C. Lo, M. Salome Rodriguez Morgade, R.K. Pandey, D.K.P. Ng, T. Torres, F. Dumoulin, The unique features and promises of phthalocyanines as advanced photosensitisers for photodynamic therapy of cancer, Chem. Soc. Rev. 49 (4) (2020) 1041–1056.
[24] X. Li, B.Y. Zheng, M.R. Ke, Y. Zhang, J.D. Huang, J. Yoon, A tumor-pH-responsive supramolecular photosensitizer for activatable photodynamic therapy with minimal in vivo skin phototoxicity, Theranostics 7 (10) (2017) 2746–2756.
[25] Y. Jia, J. Li, J. Chen, P. Hu, L. Jiang, X. Chen, M. Huang, Z. Chen, P. Xu, Smart photosensitizer: tumor-triggered oncotherapy by self-assembly photodynamic nanodots, ACS Appl. Mater. Interfaces 10 (18) (2018) 15369–15380.
[26] X. Li, S. Yu, D. Lee, G. Kim, B. Lee, Y. Cho, B.Y. Zheng, M.R. Ke, J.D. Huang, K. T. Nam, X. Chen, J. Yoon, Facile supramolecular approach to nucleic-acid-driven activatable nanotheranostics that overcome drawbacks of photodynamic therapy, ACS Nano 12 (1) (2018) 681–688.
[27] V. Abdul Rinshad, J. Sahoo, M. Venkateswarulu, N. Hickey, M. De, P. Sarathi Mukherjee, Solvent induced conversion of a self-assembled gyrobifastigium to a barrel and encapsulation of zinc-phthalocyanine within the barrel for enhanced photodynamic therapy, Angew. Chem. Int. Ed. 62 (14) (2023) e202218226.
[28] P.H. Zhao, Y.L. Wu, X.Y. Li, L.L. Feng, L. Zhang, B.Y. Zheng, M.R. Ke, J.D. Huang, Aggregation-enhanced sonodynamic activity of phthalocyanine–artesunate conjugates, Angew. Chem. Int. Ed. 61 (5) (2022) e202113506.
[29] B.D. Zheng, Q.X. He, X. Li, J. Yoon, J.D. Huang, Phthalocyanines as contrast agents for photothermal therapy, Coord. Chem. Rev. 426 (2021) 213548.
[30] M. Ankathatti Munegowda, A. Manalac, M. Weersink, S.A. McFarland, L. Lilge, Ru (II) containing photosensitizers for photodynamic therapy: a critique on reporting and an attempt to compare efficacy, Coord. Chem. Rev. 470 (2022) 214712.
[31] X. Li, E.Y. Park, Y. Kang, N. Kwon, M. Yang, S. Lee, W.J. Kim, C. Kim, J. Yoon, Supramolecular phthalocyanine assemblies for improved photoacoustic imaging and photothermal therapy, Angew. Chem. Int. Ed. 59 (22) (2020) 8630–8634.
[32] Y. Zhou, D. Wang, Y. Zhang, U. Chitgupi, J. Geng, Y. Wang, Y. Zhang, T.R. Cook, J. Xia, J.F. Lovell, A phosphorus phthalocyanine formulation with intense absorbance at 1000 nm for deep optical imaging, Theranostics 6 (5) (2016) 688–697.
[33] M. Macháček, K.A. Carter, F. Kostelanský, D. Miranda, A. Seffouh, J. Ortega, T. Šimůnek, P. Zimčík, J.F. Lovell, Binding of an amphiphilic phthalocyanine to pre-formed liposomes confers light-triggered cargo release, J. Mater. Chem. B 6 (44) (2018) 7298–7305.
[34] Y. Qian, S. Qiao, Y. Dai, G. Xu, B. Dai, L. Lu, X. Yu, Q. Luo, Z. Zhang, Molecular-targeted immunotherapeutic strategy for melanoma via dual-targeting nanoparticles delivering small interfering RNA to tumor-associated macrophages, ACS Nano 11 (9) (2017) 9536–9549.
[35] B.A. Kamino, Y.L. Chang, Z.H. Lu, T.P. Bender, Phthalonitrile based fluorophores as fluorescent dopant emitters in deep-blue OLEDs: approaching the NTSC standard for blue, Org. Electron. 13 (8) (2012) 1479–1485.
[36] Z. Wang, S. Gai, C. Wang, G. Yang, C. Zhong, Y. Dai, F. He, D. Yang, P. Yang, Self-assembled zinc phthalocyanine nanoparticles as excellent photothermal/photodynamic synergistic agent for antitumor treatment, Chem. Eng. J. 361 (2019) 117–128.
[37] H.G. Jin, W. Zhong, S. Yin, X. Zhang, Y.H. Zhao, Y. Wang, L. Yuan, X.B. Zhang, Lesson from nature: biomimetic self-assembling phthalocyanines for high-efficient photothermal therapy within the biological transparent window, ACS Appl. Mater. Interfaces 11 (4) (2019) 3800–3808.
[38] H. Pan, S. Li, J.l. Kan, L. Gong, C. Lin, W. Liu, D. Qi, K. Wang, X. Yan, J. Jiang, A cruciform phthalocyanine pentad-based NIR-II photothermal agent for highly efficient tumor ablation, Chem. Sci. 10 (35) (2019) 8246–8252.
[39] G.G. Matlou, M. Managa, T. Nyokong, Effect of symmetry and metal nanoparticles on the photophysicochemical and photodynamic therapy properties of cinnamic acid zinc phthalocyanine, Spectrochim. Acta Mol. Biomol. Spectrosc. 214 (2019) 49–57.
[40] J.T. Ferreira, J. Pina, C.A.F. Ribeiro, R. Fernandes, J.P.C. Tome, M.S. Rodriguez-Morgade, T. Torres, Highly efficient singlet oxygen generators based on ruthenium phthalocyanines: synthesis, characterization and in vitro evaluation for photodynamic therapy, Chemistry 26 (8) (2020), 1697-1697.
[41] S.Y. Lee, C.Y. Kim, T.G. Nam, Ruthenium complexes as anticancer agents: a brief history and perspectives, Drug Des, Devel. Ther 14 (2020) 5375–5392.
[42] B. Jiang, X. Yang, Y. Liu, Y. Deng, Q. Luo, Multiscale photoacoustic microscopy with continuously tunable resolution, Opt. Lett. 39 (13) (2014) 3939–3941.
[43] D. Deng, B. Dai, J. Wei, X. Yuan, X. Yang, S. Qi, Z. Zhang, A drawer-type abdominal window with an acrylic/resin coverslip enables long-term intravital fluorescence/photoacoustic imaging of the liver, Nanophotonics 10 (12) (2021) 3369–3381.